Stripe-Like hBN Monolayer Template for Self-Assembly and Alignment of Pentacene Molecules

Valeria Chesnyak, Marc G. Cuxart,* Daniel Baranowski, Knud Seufert, Iulia Cojocariu, Matteo Jugovac, Vitaliy Feyer, and Willi Auwärter*

Metallic surfaces with unidirectional anisotropy are often used to guide the self-assembly of organic molecules along a particular direction. Such supports thus offer an avenue for the fabrication of hybrid organic–metal interfaces with tailored morphology and precise elemental composition. Nonetheless, such control often comes at the expense of detrimental interfacial interactions that might quench the pristine properties of molecules. Here, hexagonal boron nitride grown on Ir(100) is introduced as a robust platform with several coexisting 1D stripe-like moiré superstructures that effectively guide unidirectional self-assemblies of pentacene molecules, concomitantly preserving their pristine electronic properties. In particular, highly-aligned longitudinal arrays of equally-oriented molecules are formed along two perpendicular directions, as demonstrated by comprehensive scanning tunneling microscopy and photoemission characterization performed at the local and non-local scale, respectively. The functionality of the template is demonstrated by photoemission tomography, a surface-averaging technique requiring a high degree of orientational order of the probed molecules. The successful identification of pentacene's pristine frontier orbitals underlines that the template induces excellent long-range molecular ordering via weak interactions, preventing charge transfer.

1. Introduction

Molecular self-assembly on surfaces is an appealing bottom-up approach for the scalable realization of nanostructured organic –metal interfaces, as it offers precise control over the elemental composition, long-range order, and tailorable morphology.[1,2] It constitutes a highly appealing route to engineer molecular ensembles at the nanoscale, with potential applications in molecular electronics, information storage, and optoelectronic devices.[3] In particular, the realization of surface-supported arrays of highly-oriented molecules via self-assembly has attracted considerable attention, opening up pathways to catalyze on-surface reactions along non-conventional reaction paths,[4,5] or to derive single molecule properties from surface-averaging techniques such as photoemission tomography.[6,7]

To this end, various strategies have been followed, mostly relying on the adsorption of molecules on metal substrates with unidirectional anisotropy, such as low-index surfaces (e.g., (110) facets of fcc crystals)[8,9] or vicinal surfaces.[10] These can act as templates that constrain the on-surface assemblies of molecules in a controlled fashion. Alternatively, 1D supramolecular gratings[11] and oxide chains[12] were fabricated on surfaces, exposing bare metal stripes confining the positions and dynamics of adsorbed molecules. However, these approaches commonly lead to modifications of the pristine properties of molecules,

V. Chesnyak[+], M. G. Cuxart[++], K. Seufert, W. Auwärter
Physics Department, TUM School of Natural Sciences
Technical University of Munich
85747 Garching, Germany
E-mail: marc.gcuxart@imdea.org; wau@tum.de

The ORCID identification number(s) for the author(s) of this article can be found under https://doi.org/10.1002/smll.202304803

[+]Present address: Istituto Officina dei Materiali, Consiglio Nazionale delle Ricerche, S.S. 14 km 163.5 in AREA Science Park, Basovizza, Trieste 34149, Italy

[++]Present address: Instituto Madrileño de Estudios Avanzados en Nanociencia (IMDEA-Nanociencia), 28049 Madrid, Spain

V. Chesnyak[+], I. Cojocariu
Dipartimento di Fisica
Università degli Studi di Trieste
via A. Valerio 2, Trieste 34127, Italy

D. Baranowski, I. Cojocariu, V. Feyer
Peter Grünberg Institute (PGI-6)
Forschungszentrum Jülich GmbH
52428 Jülich, Germany

I. Cojocariu, M. Jugovac
Elettra-Sincrotrone
S.C.p.A. S.S 14 – km 163.5, Trieste 34149, Italy

V. Feyer
Fakultät für Physik and Center for Nanointegration Duisburg-Essen (CENIDE)
Universität Duisburg-Essen
47048 Duisburg, Germany

for example, by orbital-hybridization with substrate electrons or interfacial charge transfer, which could be undesired.[8,13] Various strategies to overcome this drawback have been explored over the past years, including the design of molecular structures suitable to electronically separate molecular moieties from the substrate, or passivation of the substrate.[14] In this context, the introduction of an ultra-thin spacer layer is a promising approach, as it enables electronic and structural decoupling of the molecules from the metallic substrate.[15–17] Hexagonal boron nitride (hBN) emerged as an ideal material to serve this purpose due to its availability in atomically thin monolayers, smoothness, large bandgap, thermal stability, and inertness.[18] In addition, when supported on metallic substrates, monolayer hBN often forms structurally or electronically corrugated moiré superlattices, which can affect the arrangement of adsorbed molecules.[18,19] Specifically, the 2D hexagonal superstructures emerging on (111)-terminated surfaces of Rh, Cu, and Ir can stabilize arrays of individual molecules and support molecular self-assemblies with distinct packing geometries.[20–26] By using facets with surface lattices of square or rectangular symmetry (e.g., Ni(100),[27] Ni(110),[28] Pd(110),[29] Mo(110),[30] Cr(110),[31] Fe(110),[32] Rh(110),[33] Pt(110)[34,35]), stripe-like, 1D moiré-like superstructures with distinct periodicities have been successfully introduced to hBN, which offer great perspectives for the fabrication of the highly-oriented molecular assemblies. Complementing such an approach, 1D-textured hBN was achieved on (337) facets emerging on a curved Rh crystal.[36] The appeal of such nanostructured surfaces for templated adsorption and surface chemistry was recognized previously,[32,36,37] for example, by anticipating a spatial variation of the chemical reactivity.[37] Nevertheless, to the best of our knowledge, the ability of 1D-patterned hBN systems to template the self-assembly of molecules has not been demonstrated to date. In contrast, 1D-patterned graphene was recently experimentally explored as support for molecular adsorbates. Graphene/Ir(110) reveals a wave-like pattern with modulation of the electronic properties, promoting the formation of uniaxially aligned sandwich-molecular wires and films,[38,39] whereas the quasi-1D moiré pattern of graphene/Rh(110) did not have a major effect on the ordering of perylenetetracarboxylic dianhydride (PTCDA) molecules.[40]

In this work, we show that the self-assembly and molecular orientation of pentacene molecules are guided along distinct directions by deposition on a 1D-patterned hBN monolayer, while the pentacene's pristine electronic properties remain largely unperturbed. The robust hBN template is fabricated by scalable chemical vapor deposition (CVD) growth of hBN on Ir(100). The template's functionality is exploited by characterizing the electronic structure of the molecules by a surface-averaging technique, namely photoemission tomography (PT), which takes advantage of the molecular alignment induced by the template. Additionally, low-temperature scanning tunneling microscopy and spectroscopy (STM/STS), low-energy electron diffraction (LEED), X-ray photoelectron spectroscopy (XPS), and angle-resolved photoemission spectroscopy (ARPES) contribute to a comprehensive characterization of the rich interfacial structure, both at the atomic and mesoscopic scale. Our analysis reveals the formation of a stoichiometric boride interface alloy upon hBN growth on Ir(100) and thus emphasizes the complexity
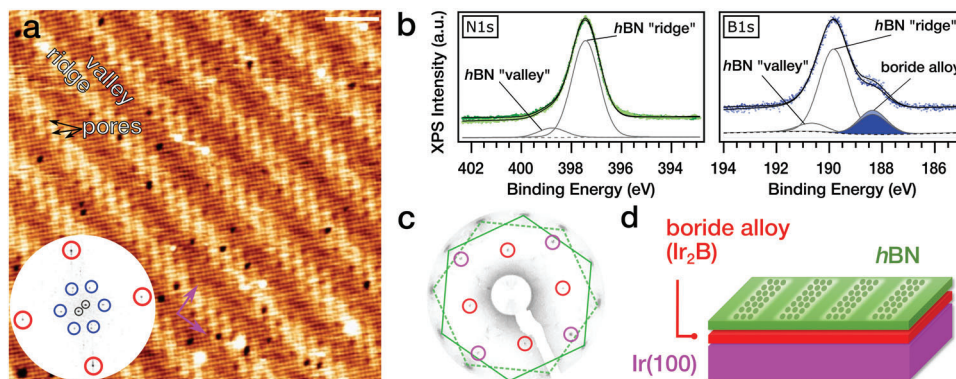
of heterostructures including 2D materials synthesized on metal supports.[41–43]

2. Results and Discussion

2.1. Growth and Structural Characterization of the 1D-Patterned Template

hBN was grown by CVD on the (100) surface of an iridium single-crystal kept at 1275 K, using borazine ($B_3N_3H_6$) under ultra-high vacuum conditions (see Section 4).[44] **Figure 1**a displays a characteristic STM image, showing an intricate surface morphology composed of three superstructures with distinct periodicities and symmetries, that are reflected in the fast Fourier transform (FFT) of the image in the inset. The most prominent superstructure consists of alternating bright and dark parallel stripes occurring with a periodicity of 4.5 nm (black circles in the FFT), which will be referred to as "ridges" and "valleys," respectively. This striped superstructure is attributed to a 1D moiré pattern emerging upon vertical stacking of symmetry-mismatched hBN and Ir(100) lattices (threefold vs fourfold symmetry, respectively).[45] Slight misalignments of the hBN lattice induce 1D moiré superstructures with different periodicities (vide infra). The second superstructure observed in the STM data (Figure 1a) consists of a quasi-hexagonal array of dips appearing within the ridge regions, that will be referred to as "pores" and are discussed in detail below. This superstructure is reflected by the six spots marked by blue circles in the FFT pattern (inset in Figure 1a). Finally, the third superstructure visible by STM consists of a square lattice with a periodicity of 0.38 nm (four spots marked by red circles in the FFT image), exceeding the lattice constant of Ir(100) (0.273 nm)[46] by a factor of $\sqrt{2}$. It results in the $c(2 \times 2)$ diffraction pattern observed by LEED (marked in red in Figure 1c), alongside the (1×1) pattern of Ir(100) (marked in purple). This superstructure is identified as an $Ir - (\sqrt{2} \times \sqrt{2}) - R45° - B$ surface reconstruction emerging from the formation of an iridium boride alloy (Ir_2B) at the Ir(100) surface, analogous to the W_2B alloy formed on W(100),[47] or the Ni_2C alloy on Ni(100) occurring in the presence of graphene.[48] Reminiscent of recent reports on alloys formed at the interface between silicene or borophene and distinct noble metal supports,[41–43] this observation of a complex interface structure upon hBN formation is a reminder of the potential intricacies in 2D materials growth that are often overlooked. The boride structure can also be observed in hBN-free areas when employing submonolayer hBN coverages (see Figure S1, Supporting Information).

Even though the honeycomb atomic lattice of hBN cannot be observed in Figure 1a because hBN appears transparent in STM under these conditions,[49,50] the presence of the hBN overlayer is confirmed by XPS and LEED. Figure 1c shows a LEED image with two sets of hexagonal diffraction patterns (highlighted in green),[51] indicating the existence of two main equivalent hBN domains rotated by 30°. Such a 30° rotation corresponds to a rotation of the moiré superstructure by 90° (see Figure S2d,e, Supporting Information). The diffraction spots of hBN have a noticeably elongated intensity profile along the tangential direction, indicating the presence of slightly misoriented (±3°) rotational hBN domains (see Figure S2, Supporting Information), whose

Figure 1. a) STM image of hBN/Ir$_2$B/Ir(100) and the corresponding FFT in the inset, depicting the periodicity of the 1D stripy pattern (black), "pore" (blue), and Ir$_2$B (red) lattices. Purple arrows indicate the [011] and [01-1] directions of the Ir(100) surface. Scanning conditions: I_t = 0.8 nA, V_b = 2.9 V, scale 5 nm. b) XPS N 1s and B 1s core level spectra, measured at normal (0°, bright green/blue data) and at grazing (70°, dark green/blue data). Fits to the data are represented by solid black lines. Minima and maxima of the grazing emission spectra have been normalized to those of the normal emission spectra for better comparison. c) LEED pattern measured at 65 eV. Diffraction features highlighted by green hexagons are attributed to hBN, by red and purple circles to Ir$_2$B alloy and Ir(100) surface respectively. d) Schematic of the layered structure.

1D corrugations are oriented in different directions, as identified by STM (Figure S3a, Supporting Information). Concomitantly, the periodicities of the template vary from about 3.6 to 4.8 nm, consistent with the expectations from simple structural models (Figure S2, Supporting Information).
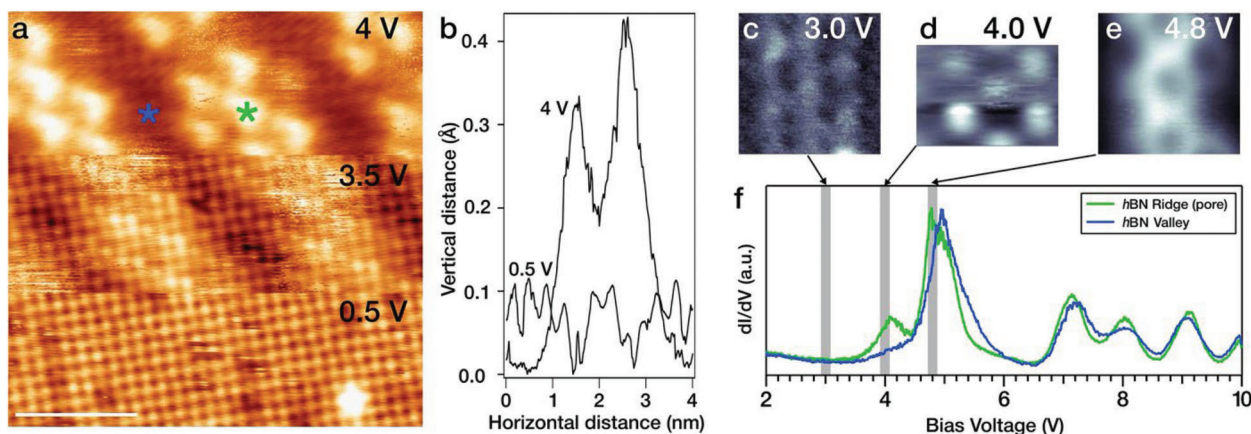
XPS measurements were performed to gain further insight into the chemical composition and morphology of the interface, including the hBN layer and the boride alloy. The N 1s core-level spectrum presented in Figure 1b shows a slightly asymmetric peak, that can be modeled by fitting two components (at 397.4 and 398.8 eV) attributed to nitrogen contained in hBN regions of distinct interfacial interaction with the substrate, as commonly reported for hBN and other metal-supported 2D materials.[52,53] This assignment is consistent with the presence of the distinct ridge and valley regions observed by constant current STM measurements at different voltages. Accordingly, the main feature in B 1s spectra can be fitted by two components owing to the same intensity ratio (at 189.8 and 190.7 eV) that leads to a B:N stoichiometry of 1: 1 (within the experimental precision of ±2%), as expected for hBN. However, the shape of the B 1s peak clearly reveals an extra component at 188.4 eV, which is attributed to the boride alloy, as it is centered at the characteristic binding energy of similar low-concentration transition metal borides.[47,54] Comparison between normal emission and grazing emission (0° and 70°, respectively) reveals an attenuation of the boride component,[49] which confirms that it is located below the hBN layer, as expected for an alloy forming at the surface of the metal substrate. A complete schematic of the layered interface structure is displayed in Figure 1d. Extended information about the emergence and stability of the boride alloy is addressed in the Supporting Information, (Figure S1), Supporting Information.

2.2. Electronic Characterization of the 1D-Patterned Template

The electronic structure of the 1D-patterned hBN template was assessed by bias-dependent STM imaging and scanning tunnel-

ing spectroscopy (STS) measurements, as shown in **Figure 2**. A sequence of STM images recorded on the same area (Figure 2a) reveals a strong bias-dependence on the apparent corrugation and contrast of the stripe-like superstructure. This is further evidenced by the line profiles taken across one such stripe presented in Figure 2b (see Figure S4, Supporting Information, for the corresponding STM images). At low bias voltages, the superstructure is not discernible but only emerges at voltages above ≈2.0 V (as revealed in Figure S4, Supporting Information), clearly indicating that the stripy 1D-pattern is of electronic rather than geometric nature. Insights into the local unoccupied electronic structure and local work function are revealed by field emission resonance (FER) measurements. These are conducted by differential conductance spectroscopy (dI/dV) reaching voltages beyond the work function, which enables access to the field emission regime (see Section 4 for more details).[55] Figure 2f compares characteristic FER spectra on the valley (blue) and pore regions (green). The former shows a sequence of resonances, the first one centered at ≈5.0 V, which is attributed to the first image potential state (IPS) and provides an approximation of the local work function.[56] A more precise value for the local work function is determined by fitting the energy positions of each resonance to the Gundlach relation,[55,57] which yields ϕ_{valley} = 4.13 ± 0.24 eV (Supporting Information, Figure S5, Supporting Information). A similar value is extracted from the ridge/pore regions (ϕ_{pore} = 4.03 ± 0.21 eV). Compared to the work function of bare Ir(100) ($\phi_{\mathrm{Ir(100)}}$ = 5.26 ± 0.13 eV), derived from FER spectra measured on bare Ir(100) as a reference (Figure S1, Supporting Information), the work function on hBN covered areas is thus reduced by 1.1–1.2 eV. This value is comparable to the work function reduction upon hBN formation on Ir(111)[24] and some coinage metals.[58,59] Despite the similar FER structures for valley and ridge regions, the latter exhibit an additional resonance at ≈4.1 V. This spectral feature is not attributed to an IPS, as it appears at too low energy and shows a low intensity, and thus is likely to be an interface state (IFS).[60,61] As shown in the dI/dV map of Figure 1d, this state is confined within the pores, suggesting a strong increase of the local interfacial interaction, in line with that reported for
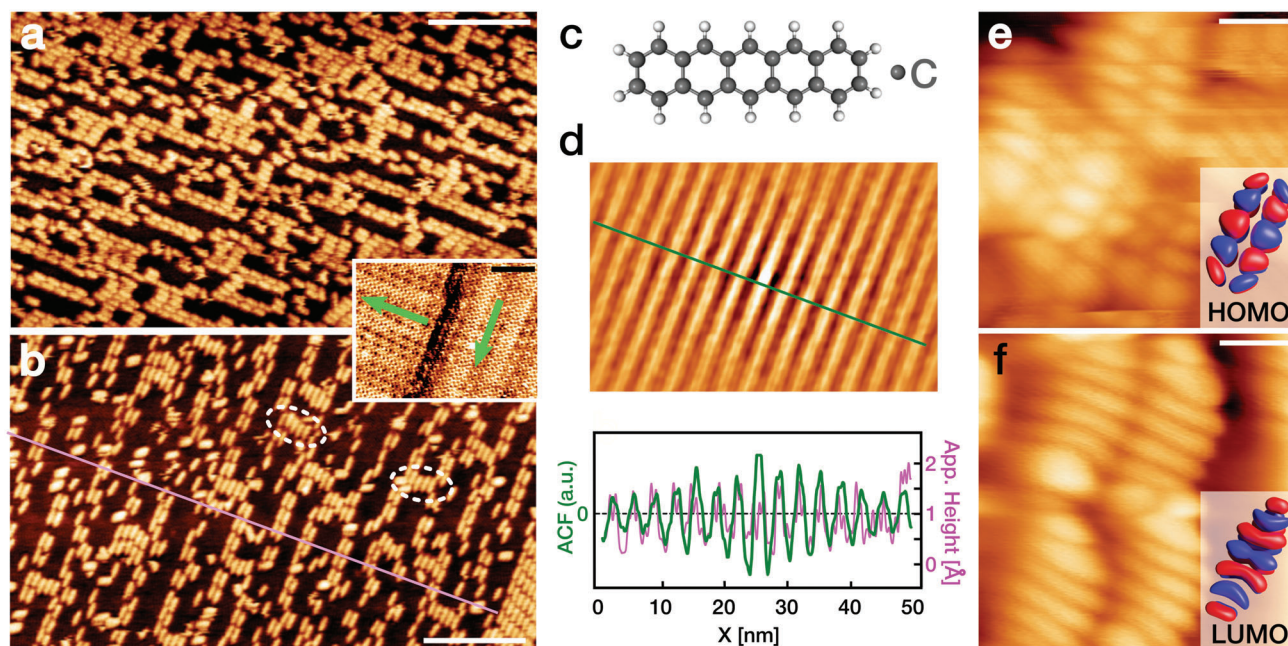
**ADVANCED
SCIENCE NEWS**

www.advancedsciencenews.com

**NANO · MICRO
small**

www.small-journal.com

Figure 2. a) High-resolution STM topographic images measured on the same region of hBN/Ir$_2$B/Ir(100) at different bias voltages ($I_t = 2$ nA, scale bar 5 nm). b) Line profile drawn along the STM image at $V_b = 0.5$ and 4.0 V (its exact position is shown in Figure S4, Supporting Information). c–e) dI/dV maps of a ridge at $V_b = 3.0$, 4.0, and 4.8 V ($I_t = 0.8$ nA, 3 nm width). f) FER measured on the pore and the valley regions of the hBN layer (see star symbols in (a)); lock-in modulation voltage: 100 mV (peak-to-peak).

spatially modulated IFS between hBN (or other 2D materials) and specific metal supports.[58,62,63]

2.3. 1D-Templated Self-Assembly of Pentacene Molecules

The periodic modulation of the electronic structure across the ridge and valley regions introduced above suggests that this system might be effectively used as a template for molecules promoting orientational order and longitudinal self-assembly. To explore this potential functionality, we deposited a sub-monolayer of pentacene (i.e., all molecules being in direct contact with hBN, while still some hBN areas remain exposed, **Figure 3**c) on the hBN template at room temperature (see Section 4). Figure 3a,b shows that pentacene molecules self-assemble, forming linear arrays along the longitudinal axis of the 1D-patterned template.

Figure 3. STM images of pentacene on hBN showing two perpendicular rotational domains. a) $I_t = 38$ pA, $V_b = 2.8$ V, and b) $I_t = 27$ pA, $V_b = 2.7$ V (scale bars: 10 nm), and a domain boundary in the inset ($I_t = 350$ pA, $V_b = 1.6$ V, scale bar: 4 nm). The red cross highlights the orientation of the boride lattice. Around 10% of the molecules in (b) appear misaligned along the fast scanning direction due to interaction with the tip. The dashed ellipses in (b) highlight molecules bridging two adjacent rows. c) Schematic of the chemical structure of pentacene, $C_{22}H_{14}$. d) Auto-correlated image and function taken from (b). Pink and green line profiles are measured along the straight lines depicted in (b) and (d), respectively. High-resolution STM topographic images of the same cluster of pentacene molecules measured at e) $I_t = 39$ pA, $V_b = -2.2$ V and f) $I_t = 50$ pA, $V_b = 2.2$ V (scale bars: 6 Å). Note that molecules slightly moved during scanning.

**ADVANCED
SCIENCE NEWS**

www.advancedsciencenews.com

**NANO · MICRO
small**

www.small-journal.com

Additionally, in these images, the orientation of the individual pentacene molecules appears locked along the direction of the linear arrays, that is, it follows the stripy corrugation of the template. The substrate clearly guides these assemblies, as they are found in distinct orientations. For example, the inset of Figure 3 reveals two perpendicular orientations, aligned along two equivalent *h*BN domains discussed above. At the pentacene coverage shown in Figure 3a,b, the linear arrays have a typical width of one or two molecules. To gain insight into the lateral separation between these linear arrays and to check if they occur with a distinct periodicity, a 2D autocorrelation function (ACF) is applied to the STM image in Figure 3b. The resulting ACF plot (Figure 3d) and the corresponding line profile clearly reveal a regular stripe-like pattern with a periodicity of about 3.8 nm. Additionally, the shallow decay of ACF intensity with distance confirms the long-range order of the pentacene assembly within the large *h*BN domain (Figure 3d).[64] The periodicity of 3.8 nm falls well into the allowed range of periodicities of the 1D superstructures (valley and ridges) emerging upon slight azimuthal rotations of *h*BN (2.2–4.8 nm, see Figure S2, Supporting Information). Indeed, an extended ACF analysis of different *h*BN rotational domains reveals periodicities ranging from 2.2 to 4.2 nm and a high orientational order of pentacenes (see Figure S6, Supporting Information). These findings confirm that the 1D-patterned *h*BN/Ir(100) system indeed works as a template promoting unique pentacene orientations in linear molecular arrays.

The molecules were easily moved by the tip during scanning, which made the simultaneous imaging of molecules and *h*BN substrate with atomic resolution extremely challenging, thus impeding the precise determination of the adsorption registry of pentacene on *h*BN. Nonetheless, images representing a low pentacene coverage strongly suggest a preferred occupation of the ridge regions, with a distinct interaction with the pore sites (see Figure S3c,d, Supporting Information). At higher coverage and in areas where the local molecular density is sufficiently high, pentacene also forms "bridges," partially filling the previously bare (valley) areas (see ellipses in Figure 3b). In this configuration, the minimal lateral distance between molecules (measured from the centers of the backbones) is 6.0 ± 0.1 Å, which suggests weak van der Waals intermolecular interaction, thus preventing the formation of pentacene-related dispersive bands. No difference in the apparent height of molecules occupying ridges and valleys is observed under the applied bias conditions, in agreement with assigning an electronic origin to the 1D-pattern.

Even though the formation of linear arrays of pentacene molecules is undoubtedly attributed to the electronically corrugated 1D *h*BN template, we venture to rationalize the underlying self-assembly mechanism in a tentative, schematic three-step model. In the initial stage of the growth (i.e., at very low molecular coverage), the adsorption of molecules is selectively dictated by the pores (see Figure S3c,d, Supporting Information), which are the regions with a distinct electronic structure, characterized by increased *h*BN/substrate interfacial interactions, as proved by the presence of the IFS (Figure 2f).[62] This pinning effect is thus not governed by in-plane electric fields created by the subtle variations of the local work function (Figure 2f).[20,26,65] Once the available pores are saturated by pentacene, these can serve as nucleation sites for additional molecules, aggregating via weak inter-

molecular van der Waals interactions.[17] The resulting assemblies are preferably constrained to the ridge regions due to the local occurrence of the pores, thus yielding linear pentacene arrays. In the later stage of growth (i.e., at molecular coverages roughly exceeding half of a monolayer), when the ridge areas are saturated, molecules also occupy valleys, hence connecting some of the linear arrays to form densely packed pentacene islands. The unique orientation of pentacene is presumably induced in the first step of pinning the molecules at the pores, whose orientation is locked regardless of the orientation of the 1D pattern (see Figure S3a, Supporting Information). As shown in Figure S3b, Supporting Information, the orientation of molecules adsorbed on slightly rotated *h*BN domains is locked, regardless of the orientation of the 1D pattern, thus indicating that the pores on the ridges play a dominant role. Indeed, the STM experiments reveal that the resulting pentacene orientations deviate by 45° from the boride lattice directions (see inset in Figure 3a,b) and thus follow the Ir <011> directions (compare Figure S2b, Supporting Information).
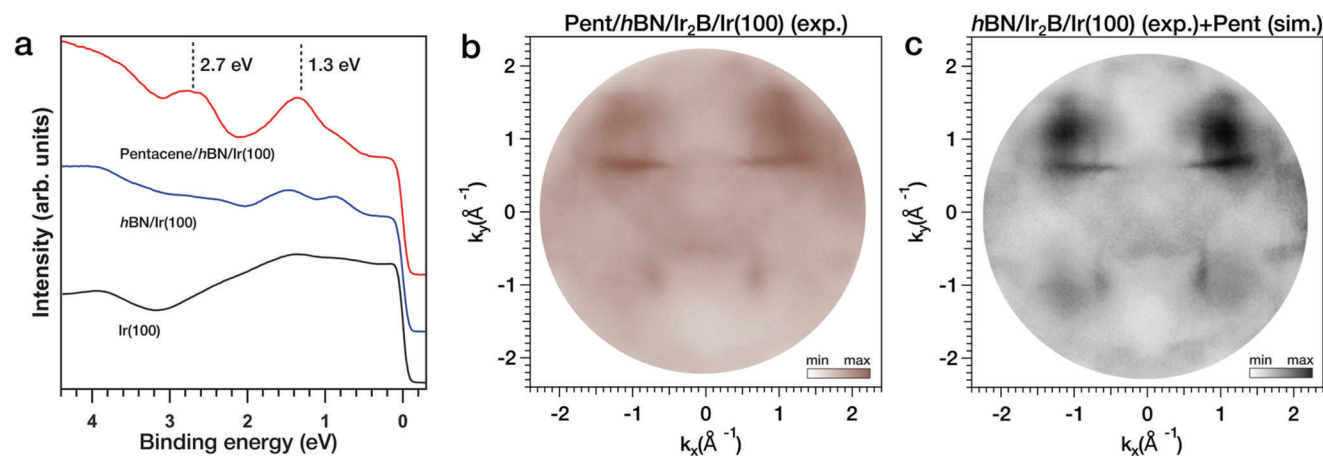
For completeness, we briefly discuss how the templated adsorption of pentacene presented here compares to pentacene adsorption on non-patterned bulk (or multilayer) *h*BN substrates. Within the sub-monolayer, pentacene typically adsorbs in a rather planar geometry,[66] forming diverse rotational (and even mirror) domains of aligned molecules that follow the threefold symmetry of the support.[67] However, such geometry is only promoted on *h*BN substrates with atomically smooth surfaces and low density of defects—perquisites that are inherently fulfilled in the monolayer case presented in this study. Low-quality *h*BN substrates can also induce a transition to an upright phase or formation of diverse film morphologies at the multilayer regime, instead of preserving the horizontally aligned pentacene phases.[67] This suggests that the highly oriented pentacene arrays formed on the 1D *h*BN template under study may also uphold the directional order in the multilayer scenario.[66,68]

2.4. Electronic Properties of Pentacene on the 1D-Patterned Template

To evaluate the interfacial interactions between pentacene and the 1D-patterned *h*BN template, the electronic structure at the single-molecule level was assessed. STM images with enhanced spatial resolution were recorded using a pentacene-functionalized tip, which allowed the visualization of the frontier orbitals. Such functionalization is achieved by picking up a pentacene molecule with the metallic STM tip, as reported in ref. [15]. The characteristic signatures of the highest occupied molecular orbital (HOMO) and lowest unoccupied molecular orbital (LUMO) of pentacene were observed at negative and positive bias voltage, respectively (STM images in Figure 3e,f),[69] thus indicating that no charge transfer between pentacene and the underlying template occurred.

Complementing the local STM measurements, we employed space-averaging photoemission experiments. Momentum-integrated valence band spectra of a pentacene monolayer on the *h*BN template, presented in **Figure 4**a, show two pronounced contributions at binding energies of about 1.3 eV and 2.7 eV. These spectral features are attributed to pentacene, as they are

ADVANCED
SCIENCE NEWS
www.advancedsciencenews.com

NANO · MICRO
small
www.small-journal.com

Figure 4. a) Angle-integrated valence band spectra (vertically offset) taken with p-polarized light at a photon energy of 30 eV for bare Ir(100), the hBN template (i.e., hBN/Ir$_2$B/Ir(100)) and pentacene deposited on the hBN template. 2D momentum maps at binding energy 1.3 eV b) measured on pentacene on the hBN template and c) obtained by combining linearly the intensity of the momentum map measured for the clean hBN template and the simulation of gas phase pentacene performed by kMap.py[70] (see Figure S7, Supporting Information).

absent in reference measurements on the bare hBN template and on Ir(100) (see Figure 4a). To assign the peaks to the molecular orbitals they originate from, we applied the PT. Importantly, the orientational alignment of the pentacene molecules induced by the 1D-patterned template opens the opportunity to employ the PT method, thus achieving insights into the occupied electronic structure of pentacene and its interfacial interactions averaging over large surface areas.[6] Within the PT approach, the square modulus of the Fourier transform of the real space molecular orbitals can be directly related to the measured momentum distribution of the photoemitted electrons (momentum map) at selected binding energies.[6] Figure 4b shows the momentum map acquired at 1.3 eV binding energy, corresponding to that of the highest occupied molecular orbital (compare Figure 4a). For comparison, Figure 4c presents a simulated momentum map, which represents a linear combination based on the gas-phase pentacene HOMO (computed by density functional theory (DFT)) and the experimental map of the bare support (i.e., hBN/Ir$_2$B/Ir(100)). The individual momentum maps used for this linear combination are displayed separately in Figure S7, Supporting Information. Here, two distinct pentacene orientations, following the high-symmetry directions of the fourfold symmetric Ir(100) substrate, and thus perpendicular to each other, were used. The excellent match between the experimental data (Figure 4b) and the simulated map (Figure 4c) lets us conclude that the highest occupied molecular orbital at a binding energy of 1.3 eV indeed represents the HOMO of gas-phase pentacene, corroborating the interpretation of the STM data (Figure 3e). From a map calculated assuming fully p-polarized light (see Methods), we determine that the molecules are aligned along the [011] and [01-1] directions of Ir(100), in agreement with the molecular orientations observed by STM.
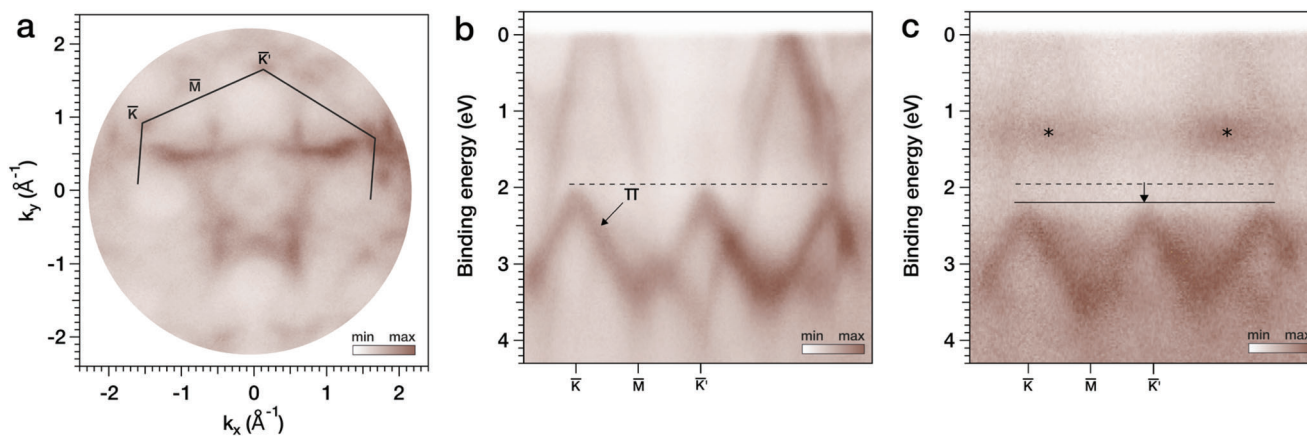
No contribution from the LUMO is observed in the valence band measurement in Figure 4a, in agreement with the real-space identification provided by STM at negative voltages (Figure 3e), confirming the absence of charge transfer between pentacene and the hBN-terminated support. Indeed, charge transfer from underlying metal supports is commonly

suppressed for pentacene adsorbed on ultrathin spacer layers, such as KCl or NaCl,[15,26] graphene,[71,72] and hBN.[26,73] In contrast, pentacene molecules adsorbed on most metallic substrates undergo charge transfer processes.[6,13,74,75] Even when applying spacer layers, charge transfer can be promoted by pronounced work function changes induced by the dielectric material, affecting the energy level alignment, as demonstrated for pentacene/MgO/Ag(001).[75] Clearly, such a scenario does not apply in the present system, where no charge transfer is detected. In addition, the energy difference between HOMO and HOMO-1 determined by photoemission (≈1.4 eV, see Figure 4a) is in good agreement with the calculated gas phase value (1.48 eV),[76] further supporting the efficient electronic decoupling by the presented 1D hBN template.

After clarifying the effect of the hBN-terminated substrate on the pentacene adsorption, we briefly address changes in the hBN induced by the molecular overlayer. To this end, **Figure 5** compares ARPES data of the bare hBN/Ir$_2$B/Ir(100) support to the pentacene-covered template. For the bare template, intensity maps acquired along the surface Brillouin zone contour of hBN (black path in Figure 5a) prominently feature the parabolic dispersive π band of hBN, with its top at a binding energy of ≈2.1 eV at the $\bar{K}$ and $\bar{K}'$ points.[77] After the deposition of pentacene, the momentum map (Figure 5c) reveals two distinct modifications. First, non-dispersive features emerge at binding energies of ≈1.3 and 2.7 eV, reflecting the pentacene HOMO (highlighted by two asterisks) and HOMO-1 earlier identified in Figure 4a. Second, a rigid shift of the hBN π bands by ≈250 meV toward higher binding energy occurred, which cannot be rationalized in terms of orbital hybridization,[78–80] hence it is tentatively attributed to work function modification induced by the adsorbed pentacene.[75,81]

3. Conclusions

In summary, we introduced a 1D-patterned template that effectively guides the self-assembly and orientational alignment of a prototypical π-conjugated molecule, namely pentacene, concurrently leaving the molecular electronic structure mostly

**ADVANCED
SCIENCE NEWS**

www.advancedsciencenews.com

NANO · MICRO

small

www.small-journal.com

Figure 5. a) 2D momentum map acquired at binding energy 1.3 eV for the hBN template (i.e., hBN/Ir$_2$B/Ir(100)). Black solid lines in (a) indicate the parallel momentum k$_{//}$ cuts presented in (b) for the hBN template and (c) for pentacene deposited on the hBN template. Asterisks highlight the position of the pentacene HOMO and dashed/solid horizontal lines the maxima of the hBN π bands. The spectra were acquired using 30 eV p-polarized photons.

unaltered. The template consists of an hBN monolayer grown by CVD on Ir(100), with characteristic, stripe-like superstructures with typical periodicities of ≈4 nm observed by STM, being a consequence of the symmetry reduction upon stacking the threefold symmetric hBN lattice on the fourfold symmetric Ir(100) surface. Concomitantly, an interfacial c(2 × 2) boron reconstruction on Ir(100) is formed below the hBN, as shown by STM, XPS, and LEED. This finding stresses the relevance of in-depth, multi-method studies to identify unexpected phases potentially arising in the CVD growth processes of 2D materials. Spectroscopic STM measurements indicate that the apparent corrugation in the 1D-patterned template is mainly of electronic origin. Deposition of pentacene molecules leads to site-selective adsorption and formation of linear arrays of equally oriented molecules that follow the 1D-patterned template. The preferential alignment of the molecules enables their characterization by orientation-sensitive, surface-averaging techniques. Specifically, photoemission tomography reveals that pentacene preserves its native charge state upon adsorption. The absence of interfacial charge transfer is corroborated by orbital-resolved STM imaging of individual pentacenes. Overall, we introduced a functional nanopatterned template with the potential to order and align individual molecules over large areas, guide supramolecular assemblies, and promote the growth and directed synthesis of 1D architectures, such as oligomers or metal-organic wires. In addition, this hBN-terminated support is expected to preserve the intrinsic electronic, magnetic, and catalytic properties of adsorbates by suppressing interfacial hybridization, charge transfer, and conformational adaptation. Achieving orientational order on mesoscopic length scales further opens pathways to retrieve information only accessible by the application of space-averaging surface science techniques.

4. Experimental Section

Sample Preparation: The Ir(100) single crystal was cleaned by several cycles of sputtering (Ar$^+$ ions at an energy of 0.8 keV) and resistive annealing at 1000 °C. hBN was grown through CVD of ≈1.8 L (2 × 10^{-8} mbar,

2 min) borazine on Ir(100) while the sample was kept at a temperature of 1000 °C. Borazine from a commercial supplier was used (Katchem spol. s.r.o., Prague, Czech Republic, www.katchem.cz/en). The hBN growth in the XPS and STM setups was conducted following the same procedure, including the use of the same heating and temperature reading devices, precursor dosing system, and chamber geometry. In the UPS/ARPES setup, the growth duration was adapted to yield the same coverage as in the XPS system, using the N 1s and B 1s XPS signals as reference. With the hBN growth being self-limited at monolayer coverage, it was ensured that a full hBN monolayer was achieved in the different experimental stations used. Pentacene molecules were purchased from Sigma-Aldrich (99%). The molecules were degassed and evaporated from a Knudsen cell (kept at 200 °C) onto hBN/Ir$_2$B/Ir(110) kept at room temperature. The pentacene monolayer is defined as the coverage where the amount of molecules is sufficient to fully cover the underlying hBN layer without formation of pentacene multilayer domains. Accordingly, the sub-monolayer regime corresponded to a situation in which all molecules were in direct contact with hBN while some hBN areas remained exposed. In the STM setup, the pentacene coverage was determined by STM imaging and the deposition times were chosen to achieve sub-monolayer coverages. To ensure that the experiments in the UPS/ARPES setup were performed at comparable coverages, specifically in the sub-monolayer regime, a calibration procedure was followed. The deposition time was calibrated by growth of a full pentacene monolayer on Ag(100) as a reference. A reduced deposition time was then applied on hBN that, jointly with a lower sticking coefficient on hBN, should guarantee a pentacene sub-monolayer coverage on hBN probed by UPS/ARPES. After preparation, the sample was cooled down before measurement by the characterization techniques presented below.

STM and STS Measurements: STM and STS measurements were performed using a commercial CreaTec LT-STM operating at 6 K and P_{base} < 2 × 10^{-10} mbar. STM images were taken at constant current mode and processed using the WSxM and Gwyddion[82] software. FER measurements were taken with the feedback loop closed (i.e., constant current mode), in order to ensure tip and sample stability, and using the lock-in technique with a modulation voltage of 100 mV at 961 Hz with tunneling currents stated in figure captions. In a separate chamber, core-level XPS measurements were performed using a commercial SPECS XPS setup, consisting of a SPECS PHOIBOS 100 hemispherical electron analyzer and an Al K_α anode as X-ray source (E_α = 1253.6 eV), calibrated using the energy position of the Ag 3d$_{5/2}$ peak measured on a clean Ag(111) single-crystal as a reference. XPS measurements were performed at room temperature and P_{base} = 1 × 10^{-9} mbar. XPS data analysis was carried out utilizing the XPST macro for IGOR (M. Schmid, Philipps University Marburg), using Voigt-like functions (Gauss-Lorentzian ratio of 0.1).

**ADVANCED
SCIENCE NEWS**

www.advancedsciencenews.com

**NANO · MICRO
small**

www.small-journal.com

Valence Band and Tomographic Photoemission Measurements: Valence band and tomographic photoemission measurements with a total resolution (analyzer + beamline) of 100 meV were carried out at the NanoESCA beamline of Elettra synchrotron. The electrostatic k-PEEM setup is summarized in ref. [83]. The measured momentum maps were acquired with a polarization slightly deviating from perfect vertical polarization, thus inducing a slight left-right intensity asymmetry. Beam-induced damage and molecular desorption were avoided by continuous rastering of the sample area. All measurements were performed with the sample kept at 90 K.

Supporting Information

Supporting Information is available from the Wiley Online Library or from the author.

Conflict of Interest

The authors declare no conflict of interest.

Author Contributions

The project was conceived by W.A. LT-STM/STS, LEED, and XPS measurements were performed by V.C. and M.G.C. with support from K.S. ARPES, k-PEEM measurements were performed by D.B., I.C., M.J., V.F., and V.C. LT-STM/STS, XPS, and LEED data were analyzed by V.C. and M.G.C., and ARPES and K-PEEM data by D.B., I.C., and M.J. V.C., M.G.C., and W.A. wrote the manuscript with feedback from all other authors.

Data Availability Statement

The data that support the findings of this study are available from the corresponding author upon reasonable request.

[1] J. V. Barth, *Annu. Rev. Phys. Chem.* **2007**, *58*, 375.

[2] K. S. Mali, N. Pearce, S. De Feyter, N. R. Champness, *Chem. Soc. Rev.* **2017**, *46*, 2520.

[3] H. Jeong, D. Kim, D. Xiang, T. Lee, *ACS Nano* **2017**, *11*, 6511.

[4] B. Cirera, Y. i.-Q. i. Zhang, J. Björk, S. Klyatskaya, Z. Chen, M. Ruben, J. V. Barth, F. Klappenberger, *Nano Lett.* **2014**, *14*, 1891.

[5] N. Merino-Díez, J. Lobo-Checa, P. Nita, A. Garcia-Lekue, A. Basagni, G. Vasseur, F. Tiso, F. Sedona, P. K. Das, J. Fujii, I. Vobornik, M. Sambi, J. I. Pascual, J. E. Ortega, D. G. De Oteyza, *J. Phys. Chem. Lett.* **2018**, *9*, 2510.

[6] P. Puschnig, S. Berkebile, A. J. Fleming, G. Koller, K. Emtsev, T. Seyller, J. D. Riley, C. Ambrosch-Draxl, F. P. Netzer, M. G. Ramsey, *Science* **2009**, *326*, 702.

[7] P. Hurdax, C. S. Kern, T. G. Boné, A. Haags, M. Hollerer, L. Egger, X. Yang, H. Kirschner, A. Gottwald, M. Richter, F. C. Bocquet, S. Soubatch, G. Koller, F. S. Tautz, M. Sterrer, P. Puschnig, M. G. Ramsey, *ACS Nano* **2022**, *16*, 17435.

[8] M. S. Sättele, A. Windischbacher, K. Greulich, L. Egger, A. Haags, H. Kirschner, R. Ovsyannikov, E. Giangrisostomi, A. Gottwald, M. Richter, S. Soubatch, F. S. Tautz, M. G. Ramsey, P. Puschnig, G. Koller, H. F. Bettinger, T. Chassé, H. Peisert, *J. Phys. Chem. C* **2022**, *126*, 5036.

[9] I. Cojocariu, S. Carlotto, H. M. Sturmeit, G. Zamborlini, M. Cinchetti, A. Cossaro, A. Verdini, L. Floreano, M. Jugovac, P. Puschnig, C. Piamonteze, M. Casarin, V. Feyer, C. M. Schneider, *Chemistry* **2021**, *27*, 3526.

[10] J. Wang, I. Kaur, B. Diaconescu, J.-M. Tang, G. P. Miller, K. Pohl, *ACS Nano* **2011**, *5*, 1792.

[11] J. I. Urgel, S. Vijayaraghavan, D. Ecija, W. Auwärter, J. V. Barth, *Surf. Sci.* **2016**, *643*, 87.

[12] Q. Fan, J. Dai, T. Wang, J. Kuttner, G. Hilt, J. M. Gottfried, J. Zhu, *ACS Nano* **2016**, *10*, 3747.

[13] X. Yang, L. Egger, J. Fuchsberger, M. Unzog, D. Lüftner, F. Hajek, P. Hurdax, M. Jugovac, G. Zamborlini, V. Feyer, G. Koller, P. Puschnig, F. S. Tautz, M. G. Ramsey, S. Soubatch, *J. Phys. Chem. Lett.* **2019**, *10*, 6438.

[14] S. Maier, M. Stöhr, *Beilstein J. Nanotechnol.* **2021**, *12*, 950.

[15] J. Repp, G. Meyer, S. M. Stojkovic, A. Gourdon, C. Joachim, *Phys. Rev. Lett.* **2005**, *94*, 026803.

[16] P. Järvinen, S. K. Hämäläinen, K. Banerjee, P. Häkkinen, M. Ijäs, A. Harju, P. Liljeroth, *Nano Lett.* **2013**, *13*, 3199.

[17] Y. Zhao, Q. Wu, Q. Chen, J. Wang, *J. Phys. Chem. Lett.* **2015**, *6*, 4518.

[18] W. Auwärter, *Surf. Sci. Rep.* **2019**, *74*, 1.

[19] T. Tian, C.-J. Shih, *Ind. Eng. Chem. Res.* **2017**, *56*, 10552.

[20] H. Dil, J. Lobo-Checa, R. Laskowski, P. Blaha, S. Berner, J. R. g. Osterwalder, T. Greber, *Science* **2008**, *319*, 1824.

[21] S. Joshi, F. Bischoff, R. Koitz, D. Ecija, K. Seufert, A. P. Seitsonen, J. Hutter, K. Diller, J. I. Urgel, H. Sachdev, J. V. Barth, W. Auwärter, *ACS Nano* **2014**, *8*, 430.

[22] M. Iannuzzi, F. Tran, R. Widmer, T. Dienel, K. Radican, Y. Ding, J. Hutter, O. Gröning, *Phys. Chem. Chem. Phys.* **2014**, *16*, 12374.

[23] R. Forker, T. Dienel, A. Krause, M. Gruenewald, M. Meissner, T. Kirchhuebel, O. Gröning, T. Fritz, *Phys. Rev. B* **2016**, *93*, 165426.

[24] F. Schulz, R. Drost, S. K. Hämäläinen, P. Liljeroth, *ACS Nano* **2013**, *7*, 11121.

[25] T. Dienel, J. Gómez-Díaz, A. P. Seitsonen, R. Widmer, M. Iannuzzi, K. Radican, H. Sachdev, K. Müllen, J. Hutter, O. Gröning, *ACS Nano* **2014**, *8*, 6571.

[26] S. Koslowski, D. Rosenblatt, A. Kabakchiev, K. Kuhnke, K. Kern, U. Schlickum, *Beilstein J. Nanotechnol.* **2017**, *8*, 1388.

[27] R. M. Desrosiers, D. W. Greve, A. J. Gellman, *Surf. Sci.* **1997**, *382*, 35.

[28] T. Greber, L. Brandenberger, M. Corso, A. Tamai, J. Osterwalder, *e-J. Surf. Sci. Nanotechnol.* **2006**, *4*, 410.

[29] M. Corso, T. Greber, J. Osterwalder, *Surf. Sci.* **2005**, *577*, L78.

[30] M. P. Allan, S. Berner, M. Corso, T. Greber, J. Osterwalder, *Nanoscale Res. Lett.* **2007**, *2*, 94.

[31] F. Müller, S. Hüfner, H. Sachdev, *Surf. Sci.* **2008**, *602*, 3467.

[32] N. A. Vinogradov, A. A. Zakharov, M. L. Ng, A. Mikkelsen, E. Lundgren, N. Mårtensson, A. B. Preobrajenski, *Langmuir* **2012**, *28*, 1775.

[33] A. J. Martínez-Galera, J. M. Gómez-Rodríguez, *Nano Res.* **2018**, *11*, 4643.

[34] S. Achilli, E. Cavaliere, T. H. Nguyen, M. Cattelan, S. Agnoli, *Nanotechnology* **2018**, *29*, 485201.

[35] D. Steiner, F. Mittendorfer, E. Bertel, *ACS Nano* **2019**, *13*, 7083.

[36] K. Ali, L. Fernández, M. A. Kherelden, A. A. Makarova, I. Píš, F. Bondino, J. Lawrence, D. G. De Oteyza, D. Y. Usachov, D. V. Vyalikh, F. J. García De Abajo, Z. M. A. El-Fattah, J. E. Ortega, F. Schiller, *Adv. Sci.* **2021**, *8*, 2101455.

[37] M. Thaler, D. Steiner, A. Menzel, F. Mittendorfer, E. Bertel, *Phys. Rev. Res.* **2020**, *2*, 043156.

[38] S. Kraus, F. Huttmann, J. Fischer, T. Knispel, K. Bischof, A. Herman, M. Bianchi, R.-M. Stan, A. J. Holt, V. Caciuc, S. Tsukamoto, H. Wende, P. Hofmann, N. Atodiresei, T. Michely, *Phys. Rev. B* **2022**, *105*, 165405.

[39] S. Kraus, A. Herman, F. Huttmann, M. Bianchi, R.-M. Stan, A. J. Holt, S. Tsukamoto, N. Rothenbach, K. Ollefs, J. Dreiser, K. Bischof, H. Wende, P. Hofmann, N. Atodiresei, T. Michely, *J. Phys. Chem. C* **2022**, *126*, 3140.

[40] H. Guo, A. J. Martínez-Galera, J. M. Gómez-Rodríguez, *Appl. Surf. Sci.* **2023**, *620*, 156777.

[41] J. T. Küchle, A. Baklanov, A. P. Seitsonen, P. T. P. Ryan, P. Feulner, P. Pendem, T.-L. Lee, M. Muntwiler, M. Schwarz, F. Haag, J. V. Barth, W. Auwärter, D. A. Duncan, F. Allegretti, *2D Mater.* **2022**, *9*, 045021.

[42] A. B. Preobrajenski, A. Lyalin, T. Taketsugu, N. A. Vinogradov, A. S. Vinogradov, *ACS Nano* **2021**, *15*, 15153.

[43] X.-J. Weng, J. Bai, J. Hou, Y. Zhu, L. Wang, P. Li, A. Nie, B. Xu, X.-F. Zhou, Y. Tian, *Nano Res.* **2023**, *15*, 9602.

[44] F. Orlando, P. Lacovig, L. Omiciuolo, N. G. Apostol, R. Larciprete, A. Baraldi, S. Lizzit, *ACS Nano* **2014**, *8*, 12063.

[45] A. Schmidt, W. Meier, L. Hammer, K. Heinz, *J. Phys.: Condens. Matter* **2002**, *14*, 12353.

[46] D. Lerch, A. Klein, A. Schmidt, S. Müller, L. Hammer, K. Heinz, M. Weinert, *Phys. Rev. B* **2006**, *73*, 075430.

[47] F. J. Tuli, G. Peng, S. Hossain, K. Ninomiya, R. Ahmed, T. Nakagawa, S. Mizuno, *Surf. Sci.* **2021**, *713*, 121906.

[48] Z. Zou, L. L. Patera, G. Comelli, C. Africh, *Carbon* **2021**, *172*, 296.

[49] M. G. Cuxart, K. Seufert, V. Chesnyak, W. A. Waqas, A. Robert, M.-L. Bocquet, G. S. Duesberg, H. Sachdev, W. Auwärter, *Sci. Adv.* **2021**, *7*, eabk1490.

[50] J. Ducke, A. Riss, A. Perez Paz, K. Seufert, M. Schwarz, M. Garnica, A. Rubio, W. Auwärter, *ACS Nano* **2018**, *12*, 2677.

[51] F. H. Farwick Zum Hagen, D. M. Zimmermann, C. C. Silva, C. Schlueter, N. Atodiresei, W. Jolie, A. J. Martínez-Galera, D. Dombrowski, U. A. Schröder, M. Will, P. Lazic, V. Caciuc, S. Blügel, T. -L. Lee, T. Michely, C. Busse, *ACS Nano* **2016**, *10*, 11012.

[52] A. B. Preobrajenski, M. A. Nesterov, M. L. Ng, A. S. Vinogradov, N. Mårtensson, *Chem. Phys. Lett.* **2007**, *446*, 119.

[53] A. B. Preobrajenski, M. L. Ng, A. S. Vinogradov, N. Mårtensson, *Phys. Rev. B* **2008**, *78*, 073401.

[54] O. Johnson, D. J. Joyner, D. M. Hercules, *J. Phys. Chem.* **1980**, *84*, 542.

[55] J. H. Coombs, J. K. Gimzewski, *J. Microsc.* **1988**, *152*, 841.

[56] H.-C. Ploigt, C. Brun, M. Pivetta, F. Patthey, W.-D. Schneider, *Phys. Rev. B* **2007**, *76*, 195404.

[57] K. H. Gundlach, *Solid-State Electron.* **1966**, *9*, 949.

[58] S. Joshi, D. Ecija, R. Koitz, M. Iannuzzi, A. P. Seitsonen, J. Hutter, H. Sachdev, S. Vijayaraghavan, F. Bischoff, K. Seufert, J. V. Barth, W. Auwärter, *Nano Lett.* **2012**, *12*, 5821.

[59] M. Garnica, M. Schwarz, J. Ducke, Y. He, F. Bischoff, J. V. Barth, W. Auwärter, D. Stradi, *Phys. Rev. B* **2016**, *94*, 155431.

[60] A. Garcia-Lekue, T. Balashov, M. Olle, G. Ceballos, A. Arnau, P. Gambardella, D. Sanchez-Portal, A. Mugarza, *Phys. Rev. Lett.* **2014**, *112*, 066802.

[61] X. Liu, L. Wang, B. I. Yakobson, M. C. Hersam, *Nano Lett.* **2021**, *21*, 1169.

[62] B. Borca, S. Barja, M. Garnica, D. Sánchez-Portal, V. M. Silkin, E. V. Chulkov, C. F. Hermanns, J. J. Hinarejos, A. L. Vázquez De Parga, A. Arnau, P. M. Echenique, R. Miranda, *Phys. Rev. Lett.* **2010**, *105*, 036804.

[63] B. o. Wang, M. Caffio, C. Bromley, H. Früchtl, R. Schaub, *ACS Nano* **2010**, *4*, 5773.

[64] S. Pichler, M. I. Bodnarchuk, M. V. Kovalenko, M. Yarema, G. Springholz, D. V. Talapin, W. Heiss, *ACS Nano* **2011**, *5*, 1703.

[65] H. G. Zhang, J. T. Sun, T. Low, L. Z. Zhang, Y. Pan, Q. Liu, J. H. Mao, H. T. Zhou, H. M. Guo, S. X. Du, F. Guinea, H.-J. Gao, *Phys. Rev. B* **2011**, *84*, 245436.

[66] S. H. Amsterdam, T. Lamountain, T. K. Stanev, V. K. Sangwan, R. López-Arteaga, S. Padgaonkar, K. Watanabe, T. Taniguchi, E. A. Weiss, T. J. Marks, M. C. Hersam, N. P. Stern, *J. Phys. Chem. Lett.* **2021**, *12*, 26.

[67] D. Günder, K. Watanabe, T. Taniguchi, G. Witte, *ACS Appl. Mater. Interfaces* **2020**, *12*, 38757.

[68] Y. Zhang, J. Qiao, S. i. Gao, F. Hu, D. He, B. Wu, Z. Yang, B. Xu, Y. Li, Y. i. Shi, W. Ji, P. Wang, X. Wang, M. Xiao, H. Xu, J.-B. Xu, X. Wang, *Phys. Rev. Lett.* **2016**, *116*, 016602.

[69] W.-H. Soe, C. Manzano, A. De Sarkar, N. Chandrasekhar, C. Joachim, *Phys. Rev. Lett.* **2009**, *102*, 100.

[70] P. Puschnig, *Comput. Phys. Commun.* **2021**, *263*, 107905.

[71] H. T. Zhou, J. H. Mao, G. Li, Y. L. Wang, X. L. Feng, S. X. Du, K. Müllen, H. J. Gao, *Appl. Phys. Lett.* **2011**, *99*, 153101.

[72] J. Yang, K. Kim, Y. Lee, K. Kim, W. C. Lee, J. Park, *FlatChem* **2017**, *5*, 50.

[73] S. H. Amsterdam, T. Lamountain, T. K. Stanev, V. K. Sangwan, R. López-Arteaga, S. Padgaonkar, K. Watanabe, T. Taniguchi, E. A. Weiss, T. J. Marks, M. C. Hersam, N. P. Stern, *J. Phys. Chem. Lett.* **2021**, *12*, 26.

[74] D. Lüftner, T. Ules, E. M. Reinisch, G. Koller, S. Soubatch, F. S. Tautz, M. G. Ramsey, P. Puschnig, *Proc. Natl. Acad. Sci U. S. A.* **2014**, *111*, 605.

[75] M. Hollerer, D. Lüftner, P. Hurdax, T. Ules, S. Soubatch, F. S. Tautz, G. Koller, P. Puschnig, M. Sterrer, M. G. Ramsey, *ACS Nano* **2017**, *11*, 6252.

[76] P. Puschnig, Organic Molecule Database: A database for molecular orbitals of π-conjugated organic molecules based on the atomic simulation environment (ASE) and NWChem as the DFT calculator, University of Graz, Austria, **2020**.

[77] R. M. Ribeiro, N. M. R. Peres, *Phys. Rev. B* **2011**, *83*, 235312.

[78] A. Fedorov, C. S. Praveen, N. I. Verbitskiy, D. Haberer, D. Usachov, D. V. Vyalikh, A. Nefedov, C. Wöll, L. Petaccia, S. Piccinin, H. Sachdev, M. Knupfer, B. Büchner, S. Fabris, A. Grüneis, *Phys. Rev. B* **2015**, *92*, 125440.

[79] S. Ichinokura, A. Hemmi, H. Cun, K. Tanaka, R. Shimizu, T. Hitosugi, T. Greber, T. Hirahara, *Appl. Phys. Lett.* **2023**, *122*, 071601.

[80] N. I. Verbitskiy, A. V. Fedorov, G. Profeta, A. Stroppa, L. Petaccia, B. Senkovskiy, A. Nefedov, C. Wöll, D. Y. u. Usachov, D. V. Vyalikh, L. V. Yashina, A. A. Eliseev, T. Pichler, A. Grüneis, *Sci. Rep.* **2015**, *5*, 17700.

[81] G. Witte, S. Lukas, P. S. Bagus, C. Wöll, *Appl. Phys. Lett.* **2005**, *87*, 263502.

[82] D. Nečas, P. Klapetek, *Cent. Eur. J. Phys.* **2012**, *10*, 181.

[83] C. M. Schneider, C. Wiemann, M. Patt, V. Feyer, L. Plucinski, I. P. Krug, M. Escher, N. Weber, M. Merkel, O. Renault, N. Barrett, *J. Electron Spectrosc. Relat. Phenom.* **2012**, *185*, 330.